Concurrent polarization retrieval in multi-heterodyne scanning near-field optical microscopy: validation on silicon form-birefringent grating

L. Yu,[1,*] T. Sfez,[1] V. Paeder,[1] P. Stenberg,[2] W. Nakagawa,[3] M. Kuittinen,[2] and H. P. Herzig[1]

[1]*Optics and Photonics Technology Laboratory, École Polytechnique Fédérale de Lausanne (EPFL), Rue A. –L. Breguet 2, CH-2000 Neuchâtel, Switzerland*
[2]*Department of Physics and Mathematics, University of Eastern Finland, P.O. Box 111, FI-80101 Joensuu, Finland*
[3]*Electrical & Computer Engineering, Montana State University, P.O. Box 173780, Bozeman, MT 59717-3780, USA*
[*]*libo.yu@epfl.ch*

Abstract: We demonstrate a concurrent polarization-retrieval algorithm based on a multi-heterodyne scanning near-field optical microscopy (MH-SNOM) measurement system. This method relies on calibration of the polarization properties of the MH-SNOM using an isotropic region of the sample in the vicinity of the nanostructures of interest. We experimentally show the effectiveness of the method on a silicon form-birefringent grating (FBG) with significant polarization diversity. Three spatial dimensional near-field measurements are in agreement with theoretical predictions obtained with rigorous coupled-wave analysis (RCWA). Pseudo-far-field measurements are performed to obtain the effective refractive index of the FBG, emphasizing the validity of the proposed method. This reconstruction algorithm makes the MH-SNOM a powerful tool to analyze concurrently the polarization-dependent near-field optical response of nanostructures with sub wavelength resolution as long as a calibration area is available in close proximity.

©2012 Optical Society of America

OCIS codes: (120.0120) Instrumentation, measurement, and metrology; (110.5405) Polarimetric imaging.

References and links

1. D. W. Pohl, W. Denk, and M. Lanz, "Optical stethoscopy: image recording with resolution λ/20," Appl. Phys. Lett. **44**(7), 651–653 (1984).
2. A. Lewis, M. Isaacson, A. Harootunian, and A. Muray, "Development of a 500 Å spatial resolution light microscope: I. light is efficiently transmitted through λ/16 diameter apertures," Ultramicroscopy **13**(3), 227–231 (1984).
3. A. Harootunian, E. Betzig, M. Isaacson, and A. Lewis, "Super-resolution fluorescence near-field scanning optical microscopy," Appl. Phys. Lett. **49**(11), 674–676 (1986).
4. E. Betzig, M. Isaacson, and A. Lewis, "Collection mode near-field scanning optical microscopy," Appl. Phys. Lett. **51**(25), 2088–2090 (1987).
5. D. Courjon, J.-M. Vigoureux, M. Spajer, K. Sarayeddine, and S. Leblanc, "External and internal reflection near field microscopy: experiments and results," Appl. Opt. **29**(26), 3734–3740 (1990).
6. N. F. van Hulst, F. B. Segerink, and B. Bölger, "High resolution imaging of dielectric surfaces with an evanescent field optical microscope," Opt. Commun. **87**(5-6), 212–218 (1992).
7. H. Bielefeldt, I. Hörsch, G. Krausch, M. Lux-Steiner, J. Mlynek, and O. Marti, "Reflection-scanning near-field optical microscopy and spectroscopy of opaque samples," Appl. Phys., A Mater. Sci. Process. **59**, 103–108 (1994).
8. B. Hecht, D. W. Pohl, H. Heinzelmann, and L. Novotny, "'Tunnel' near-field optical microscopy: TNOM-2," Ultramicroscopy **61**(1-4), 99–104 (1995).
9. M. L. Balistreri, J. P. Korterik, L. Kuipers, and N. van Hulst, "Local observations of phase singularities in optical fields in waveguide structures," Phys. Rev. Lett. **85**(2), 294–297 (2000).

#173422 - $15.00 USD Received 27 Jul 2012; revised 17 Sep 2012; accepted 18 Sep 2012; published 24 Sep 2012

10. A. Nesci, R. Dändliker, and H. P. Herzig, "Quantitative amplitude and phase measurement by use of a heterodyne scanning near-field optical microscope," Opt. Lett. **26**(4), 208–210 (2001).
11. I. Stefanon, S. Blaize, A. Bruyant, S. Aubert, G. Lerondel, R. Bachelot, and P. Royer, "Heterodyne detection of guided waves using a scattering-type scanning near-field optical microscope," Opt. Express **13**(14), 5553–5564 (2005).
12. A. Huber, N. Ocelic, D. Kazantsev, and R. Hillenbrand, "Near-field imaging of mid-infrared surface phonon polariton propagation," Appl. Phys. Lett. **87**(8), 081103 (2005).
13. B. Deutsch, R. Hillenbrand, and L. Novotny, "Near-field amplitude and phase recovery using phase-shifting interferometry," Opt. Express **16**(2), 494–501 (2008).
14. R. Esteban, R. Vogelgesang, and K. Kern, "Tip-substrate interaction in optical near-field microscopy," Phys. Rev. B **75**(19), 195410 (2007).
15. G. Lévêque, G. C. Francs, C. Girard, J. C. Weeber, C. Meier, C. Robilliard, R. Mathevet, and J. Weiner, "Polarization state of the optical near field," Phys. Rev. E Stat. Nonlin. Soft Matter Phys. **65**(3 3 Pt 2B), 036701 (2002).
16. R. Dändliker, P. Tortora, L. Vaccaro, and A. Nesci, "Measuring three-dimensional polarization with scanning optical probes," J. Opt. A, Pure Appl. Opt. **6**(3), S18–S23 (2004).
17. K. G. Lee, H. W. Kihm, J. E. Kihm, W. J. Choi, H. Kim, C. Ropers, D. J. Park, Y. C. Yoon, S. B. Choi, D. H. Woo, J. Kim, B. Lee, Q. H. Park, C. Lienau, and D. S. Kim, "Vector field microscopic imaging of light," Nat. Photonics **1**(1), 53–56 (2007).
18. M. Schnell, A. Garcia-Etxarri, J. Alkorta, J. Aizpurua, and R. Hillenbrand, "Phase-resolved mapping of the near-field vector and polarization state in nanoscale antenna gaps," Nano Lett. **10**(9), 3524–3528 (2010).
19. M. Burresi, R. J. P. Engelen, A. Opheij, D. van Oosten, D. Mori, T. Baba, and L. Kuipers, "Observation of polarization singularities at the nanoscale," Phys. Rev. Lett. **102**(3), 033902 (2009).
20. T. Sfez, E. Descrovi, L. Yu, D. Brunazzo, M. Quaglio, L. Dominici, W. Nakagawa, F. Michelotti, F. Giorgis, O. J. F. Martin, and H. P. Herzig, "Bloch surface waves in ultrathin waveguides: near-field investigation of mode polarization and propagation," J. Opt. Soc. Am. B **27**(8), 1617–1625 (2010).
21. M. Schnell, A. Garcia-Etxarri, A. J. Huber, K. B. Crozier, A. Borisov, J. Aizpurua, and R. Hillenbrand, "Amplitude- and phase-resolved near-field mapping of infrared antenna modes by transmission-mode scattering-type near-field microscopy," J. Phys. Chem. C **114**(16), 7341–7345 (2010).
22. H. W. Kihm, Q. H. Kihm, D. S. Kim, K. J. Ahn, and J. H. Kang, "Phase-sensitive imaging of diffracted light by single nanoslits: measurements from near to far field," Opt. Express **18**(15), 15725–15731 (2010).
23. R. L. Olmon, M. Rang, P. M. Krenz, B. A. Lail, L. V. Saraf, G. D. Boreman, and M. B. Raschke, "Determination of electric-field, magnetic-field, and electric-current distributions of infrared optical antennas: a near-field optical vector network analyzer," Phys. Rev. Lett. **105**(16), 167403 (2010).
24. T. Grosjean, I. A. Ibrahim, M. A. Suarez, G. W. Burr, M. Mivelle, and D. Charraut, "Full vectorial imaging of electromagneticlight at subwavelength scale," Opt. Express **18**(6), 5809–5824 (2010).
25. L. S. Goldner, M. J. Fasolka, S. Nougier, H.-P. Nguyen, G. W. Bryant, J. Hwang, K. D. Weston, K. L. Beers, A. Urbas, and E. L. Thomas, "Fourier analysis near-field polarimetry for measurement of local optical properties of thin films," Appl. Opt. **42**(19), 3864–3881 (2003).
26. P. Tortora, R. Dändliker, W. Nakagawa, and L. Vaccaro, "Detection of non-paraxial optical fields by optical fiber tip probes," Opt. Commun. **259**(2), 876–882 (2006).
27. E. Descrovi, T. Sfez, L. Dominici, W. Nakagawa, F. Michelotti, F. Giorgis, and H.-P. Herzig, "Near-field imaging of Bloch surface waves on silicon nitride one-dimensional photonic crystals," Opt. Express **16**(8), 5453–5464 (2008).
28. T. Sfez, E. Descrovi, L. Dominici, W. Nakagawa, F. Michelotti, F. Giorgis, and H.-P. Herzig, "Near-field analysis of surface electromagnetic waves in the band gap region of a polymeric grating written on a one-dimensional photonic crystal," Appl. Phys. Lett. **93**(6), 061108 (2008).
29. B. Bai, X. Meng, J. Laukkanen, T. Sfez, L. Yu, W. Nakagawa, H. Herzig, L. Li, and J. Turunen, "Asymmetrical excitation of surface plasmon polaritons on blazed gratings at normal incidence," Phys. Rev. B **80**(3), 035407 (2009).
30. E. Descrovi, T. Sfez, M. Quaglio, D. Brunazzo, L. Dominici, F. Michelotti, H. P. Herzig, O. J. F. Martin, and F. Giorgis, "Guided Bloch surface waves on ultrathin polymeric ridges," Nano Lett. **10**(6), 2087–2091 (2010).
31. T. Sfez, E. Descrovi, L. Yu, M. Quaglio, L. Dominici, W. Nakagawa, F. Michelotti, F. Giorgis, and H. P. Herzig, "Two-dimensional optics on silicon nitride multilayer: refraction of Bloch surface waves," Appl. Phys. Lett. **96**(15), 151101 (2010).
32. S. Vignolini, F. Intonti, F. Riboli, D. S. Wiersma, L. Balet, L. H. Li, M. Francardi, A. Gerardino, A. Fiore, and M. Gurioli, "Polarization-sensitive near-field investigation of photonic crystal microcavities," Appl. Phys. Lett. **94**(16), 163102 (2009).
33. Q. Tan, A. Cosentino, M. Roussey, and H. P. Herzig, "Theoretical and experimental study of a 30nm metallic slot array," J. Opt. Soc. Am. B **28**(7), 1711–1715 (2011).
34. M. Spasenović, D. van Oosten, E. Verhagen, and L. Kuipers, "Measurements of modal symmetry in subwavelength plasmonic slot waveguides," Appl. Phys. Lett. **95**(20), 203109 (2009).
35. Z. H. Kim and S. R. Leone, "Polarization-selective mapping of near-field intensity and phase around gold nanoparticles using apertureless near-field microscopy," Opt. Express **16**(3), 1733–1741 (2008).

#173422 - $15.00 USD Received 27 Jul 2012; revised 17 Sep 2012; accepted 18 Sep 2012; published 24 Sep 2012
(C) 2012 OSA

36. D.-S. Kim, J. Heo, S.-H. Ahn, S. W. Han, W. S. Yun, and Z. H. Kim, "Real-space mapping of the strongly coupled plasmons of nanoparticle dimers," Nano Lett. **9**(10), 3619–3625 (2009).
37. S. Takahashi, A. Potts, D. Bagnall, N. I. Zheludev, and A. V. Zayats, "Near-field polarization conversion in planar chiral nanostructures," Opt. Commun. **255**(1-3), 91–96 (2005).
38. R. Mohammadi, A. Unger, H. J. Elmers, G. Schönhense, M. Z. Shushtari, and M. Kreiter, "Manipulating near field polarization beyond the diffraction limit," Appl. Phys. B **104**(1), 65–71 (2011).
39. A. Ndao, Q. Vagne, J. Salvi, and F. I. Baida, "Polarization sensitive sub-wavelength metallic structures: toward near-field light confinement control," Appl. Phys. B **106**(4), 857–862 (2012).
40. B. E. A. Saleh and M. C. Teich, *Fundamentals of Photonics* (Wiley, 1991).
41. M. Born and E. Wolf, *Principles of Optics* (Cambridge University Press, Cambridge, 7th ed., 1999).
42. W. Nakagawa, R.-C. Tyan, P.-C. Sun, and Y. Fainman, "Near-field localization of ultrashort optical pulses in transverse 1-D periodic nanostructures," Opt. Express **7**(3), 123–128 (2000).
43. W. Nakagawa, R.-C. Tyan, P.-C. Sun, F. Xu, and Y. Fainman, "Ultrashort pulse propagation in near-field periodic diffractive structures by use of rigorous coupled-wave analysis," J. Opt. Soc. Am. A **18**(5), 1072–1081 (2001).
44. E. Descrovi, L. Vaccaro, L. Aeschimann, W. Nakagawa, U. Staufer, and H.-P. Herzig, "Optical properties of microfabricated fully-metal-coated near-field probes in collection mode," J. Opt. Soc. Am. A **22**(7), 1432–1441 (2005).
45. T. C. Choy, *Effective Medium Theory: Principles and Applications* (Oxford University Press, Oxford, 1999).
46. M. P. Nezhad, C. Tsai, L. Pang, W. Nakagawa, G. Klemens, and Y. Fainman, "Form birefringent retardation plates in GaAs substrates: design, fabrication, and characterization," Proc. SPIE **5225**, 69–77 (2003).
47. F. Xu, R.-C. Tyan, P.-C. Sun, Y. Fainman, C.-C. Cheng, and A. Scherer, "Form-birefringent computer-generated holograms," Opt. Lett. **21**(18), 1513–1515 (1996).

1. Introduction

Scanning near-field optical microscopy (SNOM) is a popular tool to overcome the diffraction limit for the investigation of subwavelength-scale optical structures. For nearly 30 years, various configurations have been implemented to characterize the interactions of the electromagnetic field with nanostructures in the near field [1–13]. An accurate understanding of these interactions requires a detailed knowledge of the field, including the state of polarization (SOP) in the near field. The state of polarization is easily accessible in far-field microscopy, but is challenging to measure in the near field. When the SNOM probe interacts with the near field and scatters the signal to the far field, the near-field polarization may be considerably altered [14]. Moreover, the near-field polarization may be oriented in all three dimensions [15] whereas far-field propagation implies a two-dimensional (transverse) polarization.

Recently, several phase- and polarization-sensitive measurements in the near field have been reported [16–24]. Each of the methods introduces a polarization-selective element to a SNOM configuration to obtain polarization-resolved information and reconstruct the vector field. For example, recently M. Schnell et al. [18] described interferometric detection of the near-field polarization state in nano-antenna gaps using a scattering-type SNOM (s-SNOM). M. Burresi et al. [19] observed in collection mode the polarization singularities in a 2D photonic crystal waveguide with an aperture probe. In these examples, two sequential measurements are performed to obtain information for two orthogonal polarization states, enabling reconstruction of the state of polarization observed at the sample. L. S. Goldner et al. [25] have demonstrated SNOM using a time-varying input polarization state to mitigate some of the concerns. Nevertheless, since the polarization measurements are not performed concurrently, this may introduce some measurement uncertainties due, for example, to drift from mechanical misalignment, changing condition of the probe, or time dependent phase drift.

Multi-heterodyne scanning near-field optical microscopy (MH-SNOM) [16, 20, 26–31] enables the simultaneous detection of two vector field components associated with each of two orthogonally polarized illumination beams. This provides further information about the SOP in the near field, although still does not provide the full three-dimensional SOP. In our previous work [20], we extracted concurrently from a MH-SNOM measurement the state of polarization using a polarization retrieval algorithm based on criteria predicted from

simulations. However, these criteria are applicable only if the near-field response of the nanostructure can be determined by another method.

In this paper, we strengthen the algorithm by freeing it from a priori knowledge of the fields. We use an isotropic region in the vicinity of the nanostructure as a calibration area, whose known polarization properties provide a global criterion to calibrate the polarization distortion induced by the detection system. Moreover, with a tunable laser source, this process could be iterated to calibrate the system characteristics over the desired wavelength operating range. This makes MH-SNOM a powerful polarization-resolved tool which can be applied to analyze any polarization-dependent nanostructure with subwavelength resolution, as long as an isotropic region is available in its vicinity. This method could contribute to the fundamental study of polarization-sensitive nanophotonic structures such as photonic crystal microcavities [32,33], waveguides [34], thin films [25], nanoparticles [35, 36] and other near-field polarization-sensitive imaging applications [37–39].

Due to their simplicity in terms of the near-field distribution and strong polarization dependence, form-birefringent gratings (FBG) are optimal structures to assess the polarization-retrieval algorithm proposed here. We experimentally demonstrate this algorithm by validating it in retrieving the polarization-dependent near-field distribution on a silicon FBG. Due to the symmetries inherent in this one-dimensional grating and the configuration of the illumination beam—longitudinally oriented fields with respect to the probe are not excited—the full vectorial field emitted by this structure can be detected using the MH-SNOM.

In section 2, a description of the experimental set-up is presented. Next, the polarization-retrieval algorithm used in this work is explained step by step in section 3. Then, the fabrication of the FBG is described in section 4. The results of near-field measurements are discussed in section 5: we first demonstrate the method through the retrieval of the measured near-field confinement on the FBG in three spatial dimensions. Then, pseudo-far-field measurements are performed to verify the effective refractive index of the FBG. Finally conclusions are presented in section 6.

2. Experimental set-up

Optical measurements are performed using a MH-SNOM [20]. This type of SNOM is a modified version of a classical heterodyne SNOM [10]. The light is collected with a SNOM probe (Lovalite, tapered single-mode fiber with 70 nm aluminum coating and apex aperture with diameter ~200 nm) positioned above the surface of the sample. The topography is obtained by means of a shear-force feedback system (SNOM control unit, APE Research). A collimated and linearly polarized beam at 1535.4 nm wavelength illuminates the sample through the substrate at normal incidence. The Transverse Magnetic (TM) and the Transverse Electric (TE) polarization states are respectively defined to be aligned with the grating axes as shown in Fig. 1.

#173422 - $15.00 USD Received 27 Jul 2012; revised 17 Sep 2012; accepted 18 Sep 2012; published 24 Sep 2012
(C) 2012 OSA

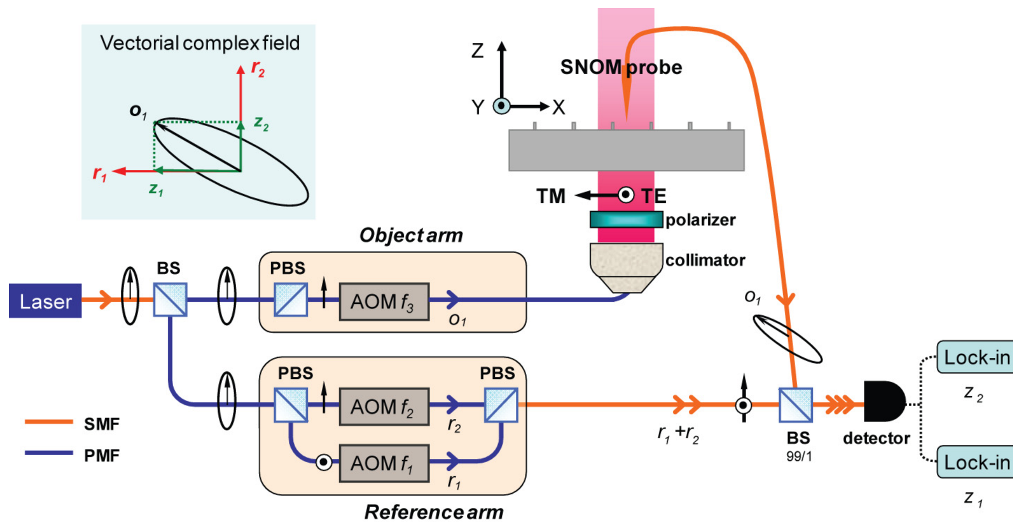

Fig. 1. Schematic diagram of the experimental MH-SNOM set-up (AOM: Acoustic Optic Modulator, SMF: Single Mode Fiber, PMF: Polarization Maintaining Fiber, BS: Beam Splitter, PBS: Polarizing Beam Splitter). Inset: object beam o_1 is projected on the reference basis $\{r_1, r_2\}$; the two resulting components are called z_1 and z_2.

In the MH-SNOM configuration used here (see Fig. 1), the reference arm is split at an amplitude ratio of 1:1 into two orthogonally polarized beams. Each of the three channels (one object channel, two reference channels) is shifted by a different frequency, using acousto-optic modulators. The orthogonality of the two reference signals r_1 and r_2 is well preserved up to the detector, where they are combined with the signal o_1 from the object beam. Due to the differing frequencies between the three signals, the projection of the object beam o_1 on the orthogonal reference basis $\{r_1, r_2\}$, called z_1 and z_2, can be detected simultaneously using two lock-in amplifiers. Thus, these two concurrently obtained phase-resolved field projections provide the full information of the optical field collected by the SNOM probe.

The challenge for MH-SNOM to resolve the state of polarization of the field on the sample lies in the polarization distortion introduced by the unknown polarization transfer function (PTF) of the aperture-probe and the fibered detection path. An unknown phase delay from the optical path difference (OPD) between the two reference arms and the unknown polarization rotation occurring in the single mode fibers (SMF) must be compensated. Assuming that the above uncertainties are stable and reproducible, the heterodyne signals captured by the detection system contain full information for the optical fields captured by the probe. Thus, rather than controlling the polarization properties of these parts of the MH-SNOM, it is possible to reconstruct the polarization signal captured by the probe, as described in the next section.

3. Polarization retrieval algorithm

The principle of the polarization retrieval algorithm is a calibration mechanism, which is introduced to quantify the polarization distortion resulting from the unknown PTF. For this purpose, we introduce a calibration element, with a known field response, to determine the PTF. In practice, the calibration element is taken to be an unstructured area of the sample in the vicinity of the nanostructure of interest. It is assumed that the linearity of the incident beam is preserved when crossing the unstructured region, owing to its isotropic nature. Using the known, presumed linear SOP in this region, we are able to compute the PTF for the specific probe being used. The computed PTF is used to compensate the corresponding SOP distortions in the measurements performed on the nanostructures for which the field response is unknown. The computed PTF can be written as a polarization transfer matrix M. Thus, the

#173422 - $15.00 USD Received 27 Jul 2012; revised 17 Sep 2012; accepted 18 Sep 2012; published 24 Sep 2012
(C) 2012 OSA

model developed in [20] to express the field at the sample surface can be expanded as follows:

$$\begin{pmatrix} E_{s,x} \\ E_{s,y} \end{pmatrix} = M^{-1} \begin{pmatrix} E_{d,r_1} \\ E_{d,r_2} \end{pmatrix} \tag{1}$$

where E_s is the field above the sample surface expressed in the basis {x, y}, and E_d is the field at the detector expressed in the basis {r_1, r_2} of the reference arm. Since any state of polarization can be reached with a proper combination of a quarter-wave plate J_4 and a half-wave plate J_2, M is rewritten as an equivalent Jones matrix:

$$M = R(-\alpha_1)J_2R(\alpha_1)R(-\alpha_2)J_4R(\alpha_2) \tag{2}$$

where R is a rotation matrix [40]. The complex matrix M is obtained by seeking the rotation angles α_1 and $\alpha_2$required in order to match the field measured above the flat area with its expected theoretical response. The algorithm of the iterative search procedure is depicted in Fig. 2.

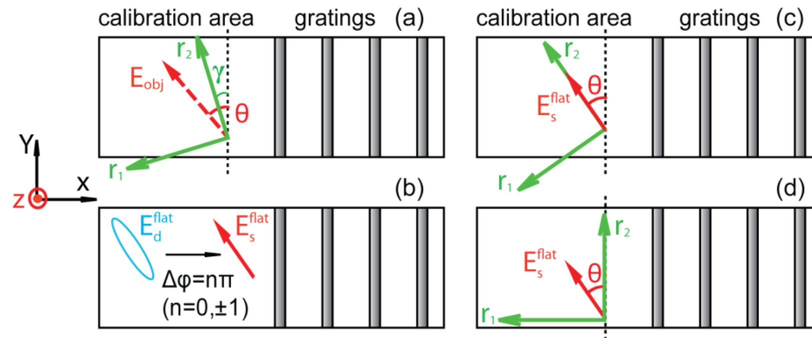

Fig. 2. Schematic illustration of the polarization-retrieval algorithm. Both the nanostructure of interest (e.g. gratings) and a flat calibration region are illuminated. (a) A collimated linearly polarized object beam E_{obj}, propagating in z, is aligned at θ = 45° with respect to the x-y axis. The fact that the reference basis {r_1, r_2} has an arbitrary orientation with respect to the object field at the detector can be equivalently represented by an arbitrary angle γ with respect to y axis. (b) Transformation of the detected field above the flat region to reconstruct the linearity of the incident beam. (c) The arbitrary location of the reference basis {r_1, r_2} is specified by aligning r_2 with the object beam. (d) The reference basis {r_1, r_2} is turned θ = 45° to the orientation of interest.

As shown in Fig. 2(a), a collimated linearly polarized object beam E_{obj}, propagating in z, is physically aligned at θ = 45° with respect to the x-y axes. The illuminated area is selected to include both the nanostructure of interest (e.g. gratings) and a flat calibration region. The fact that the reference basis {r_1, r_2} has an arbitrary orientation with respect to the object field at the detector can be approximately represented by an arbitrary angle γ at the sample plane. The optical field response is then measured. The following steps are then applied to the experimental data. First, in order to recover the linearity of the field response of the flat region $E_d^{flat}(r_1, r_2)$, the angle $\alpha_1$of the half-wave plate is kept constant while adjusting the angle $\alpha_2$of the quarter-wave plate (Fig. 2(b)). Then, in order to specify the location of the reference basis {r_1, r_2}, α_2 is kept fixed and α_1 is varied to maximize one component of the field E_d^{flat}. We seek to minimize one polarization component as this diminishes the effect of an asymmetric probe on the optimization procedure. The obtained value of α_1 ensures that one axis of the reference basis {r_1, r_2} is aligned with the object beam E_{obj} (γ = θ), as represented in Fig. 2(c). A 45° offset is then added to α_1 to align {r_1, r_2} with {x, y} (Fig. 2(d)). Thus, the

#173422 - $15.00 USD Received 27 Jul 2012; revised 17 Sep 2012; accepted 18 Sep 2012; published 24 Sep 2012
(C) 2012 OSA

obtained field components (projections of the detected signal onto the reference beams with basis $\{r_1, r_2\}$) represent the TE and TM components of the field at the sample.

The matrix M is constructed by inserting the obtained values of α_1 and α_2 into Eq. (2). It is then applied on the field measured above the structure of interest to reconstruct its complex field response. We apply this method to experimental MH-SNOM measurements in the following, with the sample being a FBG as described in the next section.

4. Form-birefringent grating

A FBG is a sub-wavelength one-dimensional periodic structure inducing a large birefringence, yielding a highly polarization-dependent behavior [41]. In the near field, this appears as a polarization-dependent field confinement. In this work, such a structure is fabricated in silicon using standard high-resolution lithography and etching processes, as described below.

A scanning electron micrograph of the form-birefringent silicon grating is shown in Figs. 3(a) and 3(b). The structure consists of a 1-D binary grating with period $\Lambda = 1$ µm, fill factor F = 7% and depth d = 300 ± 20 nm. The sample is fabricated by using electron beam (e-beam) lithography and plasma etching. A double side polished silicon wafer with 50 mm diameter and <100> crystal orientation is spin coated with a 180 nm thick layer of binary negative-tone electron beam resist. The resist used is Dow Corning® XR-1541 e-beam resist which contains hydrogen silsesquioxane (HSQ) resin in a carrier solvent of methyl isobutyl ketone (MIBK). After spin coating the sample is vacuum baked under 2×10^{-6} Torr pressure for two minutes to evaporate excess solvent. The sample is patterned with an electron beam pattern generator (Leica Vistec EBPG 5000 + ES HR). The acceleration voltage of the pattern generator is set to 100 kV and the applied dose for the pattern is 6000 $\mu C/cm^2$. The patterned sample is developed with diluted Microposit 351 developer, rinsed with 2-propanol (IPA) and finally with deionized (DI) water.

The pattern transfer into the silicon is performed with an Oxford Instruments Plasmalab 100 etching system. In silicon etching, a hydrogen bromide (HBr) based Inductively Coupled Plamsa-Reactive Ion Etch (ICP-RIE) process is used. For sidewall passivation, a small quantity of oxygen is added to achieve vertical sidewalls. Helium backside cooling is used for stabilizing the process temperature. After etching, the remaining HSQ mask is removed with a hydrogen fluoride (HF) based solution.

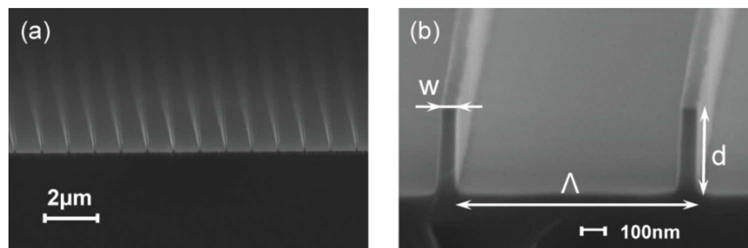

Fig. 3. (a) SEM micrograph of the fabricated 1-D binary grating.(b) Close-up view of the grating parameters: period $\Lambda = 1$ µm, ridge width w = 70nm, and depth d = 300 ± 20 nm.

This structure is designed to sustain strong transverse near-field confinement within each period of the structure at normal incidence [42, 43].

5. Results and discussion

The method described in section 3 is applied to analyze MH-SNOM measurements of the above FBG sample. The structure is illuminated through the substrate (from below) at normal incidence with a collimated beam linearly polarized at 45° with respect to the grating grooves. Polarization-resolved maps of the field measured at the surface of the FBG and in a calibration area (an unstructured region near the rating) are shown in Figs. 4(a) and 4(b). The

#173422 - $15.00 USD Received 27 Jul 2012; revised 17 Sep 2012; accepted 18 Sep 2012; published 24 Sep 2012
(C) 2012 OSA

topography is shown in Fig. 4(c), and indicates the position of the grating edge, as well as the ridges and grooves. The width of the grating ridges appears wider than expected due to the finite size and profile of the probe. As in [44], we model the probe response by a convolution with a Gaussian function $f(x) = \exp(-x^2 / 2\sigma^2)$. The parameter σ is computed by comparison of the measured topography with the expected binary structure convolved with f. Agreement is obtained with ± 2.8% error for σ = 290 nm in terms of FWHM (full width of half maximum) of the ridge structure. The value of σ corresponds to the effective diameter of the probe.

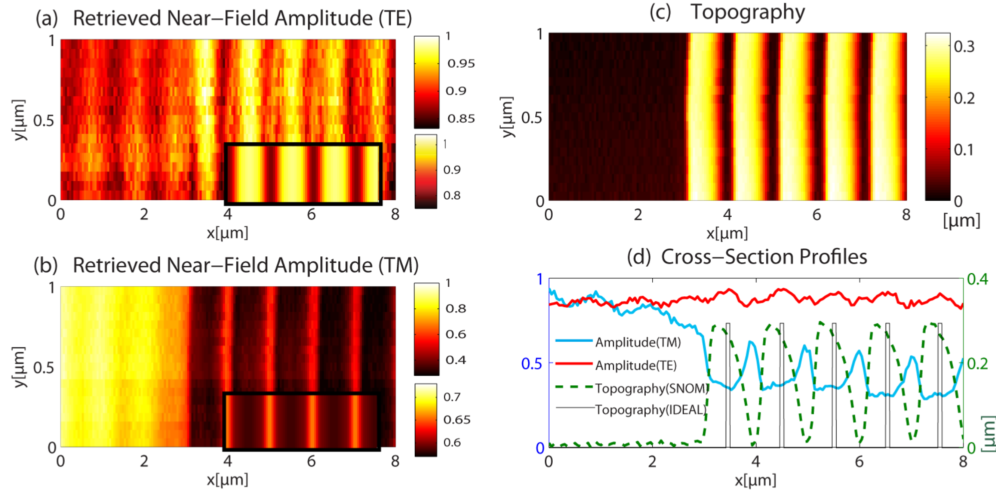

Fig. 4. MH-SNOM measurement results for the device shown in Fig. 3: the x-y maps (8 μm × 1 μm) of the retrieved near-field amplitude for (a) TE polarized and (b) TM polarized light at a wavelength of 1535.4 nm (insets show RCWA simulations of the field amplitude); (c) topography of the measured area of the sample; and (d) cross-section profiles along x of the TE and TM field amplitudes and topography, showing the polarization-dependent spatial localization of the near fields.

As predicted by the RCWA simulations, for the TE polarization (see Fig. 4(a)), the field is primarily localized in the silicon ridges, while for the TM polarization, the field is localized in the grooves (see Fig. 4(b)). The insets in Figs. 4(a) and 4(b) show the predicted field distribution in the near field, obtained by convolving the field simulated using RCWA with the probe model described above. Figure 4(d) shows a cross-section profile of the TE and TM field amplitudes along with the topography profile. This emphasizes the fact that the TE polarized fields are localized in the grating ridges, while the TM polarized fields are localized in the grating grooves, as expected in the models. In addition, we can see that the two polarization components have approximately equal amplitudes in the calibration (unstructured) region, while the TE polarization has amplitude approximately 1.3 times that of the TM in the grating region.

The fringes appearing in the flat region are attributed to the interference between the transmitted zeroth order and the first diffraction order inside the substrate (totally internally reflected on both sides of the flat interface of the bare substrate). The spatial period of the measured interference fringes ($\Lambda_f \approx 1.06$ μm ± 0.107 μm) is close to the expected value which is the period of the grating (Λ = 1 μm). Λ_f is obtained from:

$$\Lambda_f = \frac{1}{k_x} = \frac{\lambda}{n_{si} \sin\theta_1} = \Lambda \tag{3}$$

#173422 - $15.00 USD Received 27 Jul 2012; revised 17 Sep 2012; accepted 18 Sep 2012; published 24 Sep 2012
(C) 2012 OSA

Where n_{si} is the refractive index of silicon and θ_1 is the diffraction angle for the 1st reflected order inside the substrate.

5.1 Decay of the near-field confinement

Next, we assess the extent of the field localization in the grating by performing an x-z (3 µm × 300 nm) scan MH-SNOM measurement above the grating in order to investigate the decay of the near-field confinement. The results are presented in Figs. 5(a-h).

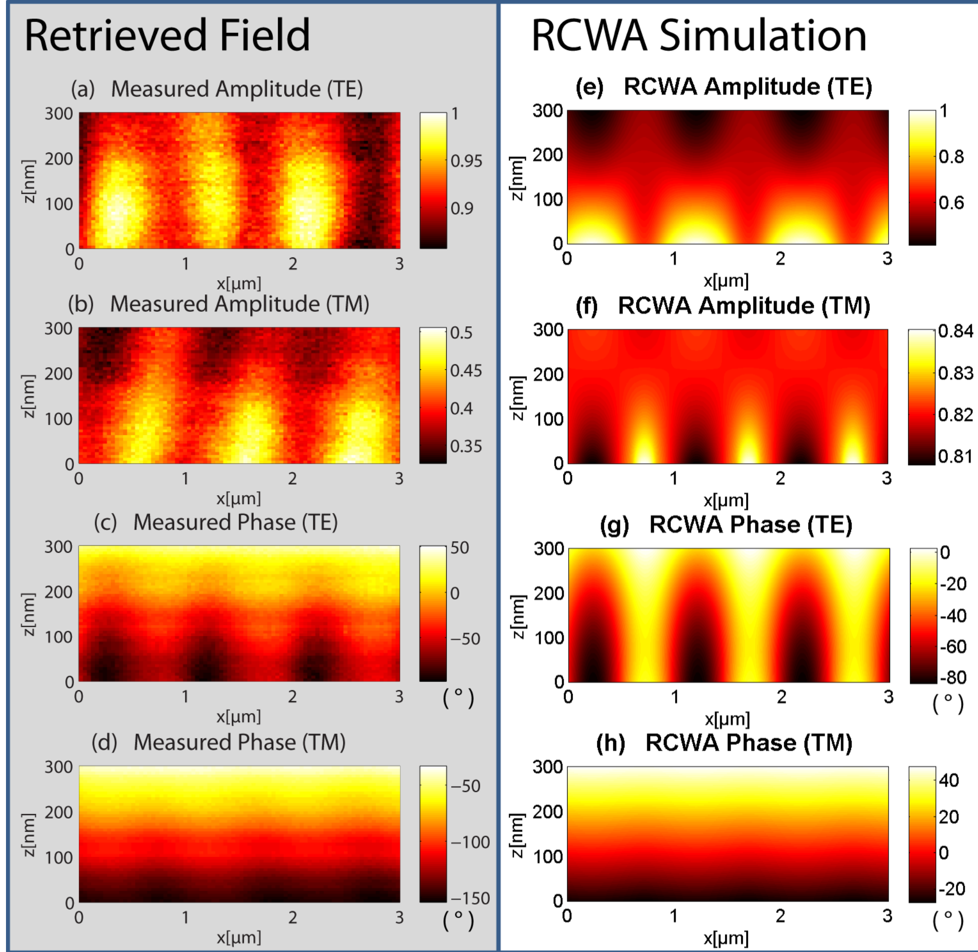

Fig. 5. MH-SNOM results for an x-z (3 µm × 300 nm) scan measuring the optical fields above the grating at 1535.4 nm wavelength: retrieved near-field amplitude and phase measurement in TE (a,c) and in TM (b,d). The RCWA simulated amplitude and phase response in TE (e,g) and in TM (f,h).

The retrieved near-field amplitude responses (TE/TM) (illustrated in Figs. 5(a) and 5(b)) exhibit a maximum respectively above the ridges and the grooves, as expected from the RCWA simulations (Figs. 5(e) and 5(f)). The phase variation in TM (Fig. 5(d)) is smaller than in TE (Fig. 5(c)) due to the weaker confinement. In both TE and TM cases, the lateral confinement of the field gradually diminishes with increasing altitude above the sample. The experimental results shown in Figs. 4(a–b) and Figs. 5(a–d) show some minor differences due to the change in scanning mode (topographic scan vs. constant height mode) and analyzing different regions of the sample (which are not necessarily identical due to fabrication tolerances), but these results are qualitatively in agreement. Comparing the experimental

#173422 - $15.00 USD Received 27 Jul 2012; revised 17 Sep 2012; accepted 18 Sep 2012; published 24 Sep 2012
(C) 2012 OSA

measurements to RCWA simulations in Fig. 5 also reveals qualitative agreement with some quantitative differences. We believe these effects are primarily due to small imperfections in both the sample and SNOM probe; for example, minor variations in the grating depth, grating width, substrate depth as well as the probe coupling characteristics could affect the detected optical signal.

To assess the decay properties of the localized evanescent modes, another scan is performed above a ridge from near the grating surface to more than half a wavelength (900 nm) above the surface. The field near the grating surface is assumed to take the form

$$E(x,z) = a_0 e^{i(k_0 z + \phi_0)} + \sum_{n \neq 0} a_n e^{i(k_{xn} x + \phi_n)} e^{-|k_{zn}| z} \quad (4)$$

where a_n is the amplitude of the n-th Rayleigh order, ϕ_n is its relative phase difference, and k_{xn} and k_{zn} are the x and z components of its wave vector, respectively.

The amplitude of the 1st evanescent order is obtained by fitting Eq. (4), truncated to the 1st order, to the measurement. The higher orders are neglected, as their decay lengths are too short to be measured accurately. The amplitude ratio of the 1st order to the 0thorder, $\rho = a_1 / a_0$, is investigated. For TE, one obtains ρ = 0.119 ± 0.043 (simulation: ρ = 0.113). Note that in the simulations, varying the substrate thickness within the fabrication tolerances has a strong impact on the relative amplitude of the modes, due to Fabry-Pérot resonances in the substrate. The substrate thickness was observed to vary by several microns over the sample area, and a specific thickness value cannot be determined. In this analysis, we assume a substrate thickness of 279.67 μm, which is consistent with the experimentally observed thicknesses.

5.2 Pseudo-far-field characterizations

By successfully reconstructing the polarization-dependent near-field localization of the optical fields in the nanoscale grating, we are able to observe directly the origins of the well-known macroscopic form-birefringence effect. From the effective medium theory (EMT) [45], if the probe were lifted a few wavelengths away from the surface, the FBG behaves as a homogeneous material. In order to emphasize the effectiveness of the algorithm as well as to verify that the values obtained using the SNOM are consistent with the predicted far-field values, the probe is raised and the SNOM measurement is extended to characterize the polarization dependence of the effective refractive indices.

In this process, the algorithm is applied to retrieve the phase difference between the phase on the grating and the phase on the flat region at a constant height. For this purpose, pseudo-far-field MH-SNOM measurements are implemented at a height of 15 μm above grating. This distance is large enough to avoid the influence of near-field effects. Moreover, it is close enough to avoid the influence of diffraction at the boundary between the grating and the flat region.

An x-z (100 μm × 2.3 μm) scan measurement is carried out. The retrieved phases of the two field components are illustrated in Figs. 6(a) and 6(b) as the phase responses of the TM/TE polarized component of the incident beam.

In Figs. 6(a-c), the left portion of the scan corresponds to the grating region, as shown in the topography in Fig. 6(c). As expected, the ridges and grooves are not distinguished. In the calibration (unstructured) region of the grating, shown in the right part of the scans in Figs. 6(a-c), the linearity of the object beam is observed. For the TE polarization (Fig. 6(b)), there is a significant phase shift between the grating region and the calibration region. In contrast, for the TM polarization (Fig. 6(a)), the phase is nearly constant. The measured effective refractive index values are thus derived from this phase difference, and found to be n_{TE} = 1.46 ± 0.021 and n_{TM} = 1.01 ± 0.018 at a wavelength of 1535.4 nm.

#173422 - $15.00 USD Received 27 Jul 2012; revised 17 Sep 2012; accepted 18 Sep 2012; published 24 Sep 2012
(C) 2012 OSA

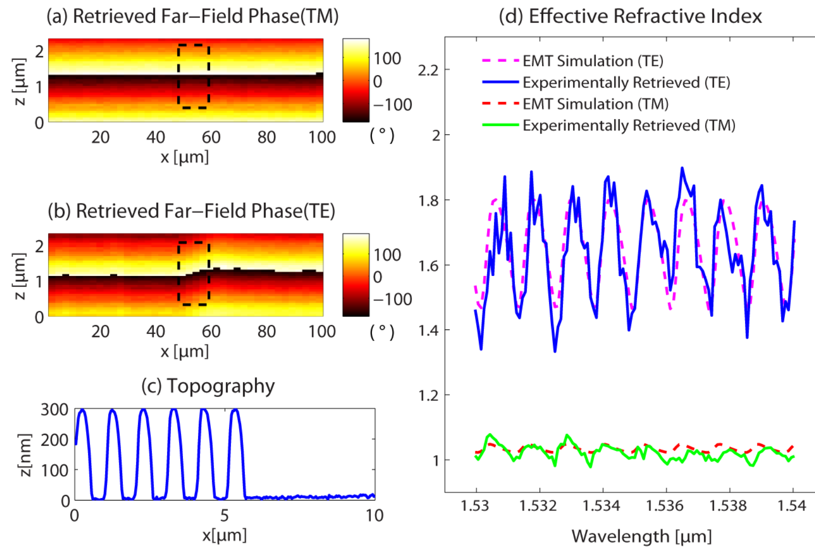

Fig. 6. (a). (b). x-z (100 μm × 2.3 μm) retrieved phase-response (TM/TE) from 15 μm above the sample at 1535.4 nm wavelength. The measured area covers both the grating and the flat region. The10 μm of the topography shown in (c) is taken from the x position indicated by the square inset in (b). (d) At a constant height of 15 μm, one line scans along x are executed while sweeping the wavelength. The wavelength is swept over 1530 nm-1540 nm with a step of 0.09 nm. For each wavelength, the obtained phases are retrieved, and the difference between the average phases on the flat area and the grating region are converted to an effective refractive index (TE/TM), shown in solid lines. For comparison, equivalent values are computed using 2nd order effective medium theory, and plotted in dashed lines.

To verify this analysis, we maintain the probe at a height of 15 μm above the sample, and perform linear scans along x while sweeping the wavelength. The wavelength is swept over the range 1530–1540 nm with a step of 0.09 nm. Retrieving the measured field using the algorithm at each wavelength, the phase differences between the grating and the calibration (unstructured) area are obtained. Converting these results into the corresponding indices of refraction, the retrieved effective indices (TE/TM) of the FBG versus wavelength are plotted in Fig. 6(d) as the solid lines. A periodic modulation as a function of wavelength appears. This is basically due to a Fabry-Perot effect: since the Si substrate has a high refractive index ($n = 3.48$) compared with the grating layer, it acts as a cavity [46]. If we compare with the second order effective medium theory [47] (Fig. 6(d) dashed lines), we find good agreement. This result demonstrates the effectiveness of the algorithm and the feasibility of characterizing the effective refractive index with this method.

6. Conclusions

In summary, we have demonstrated a polarization retrieval algorithm which enables the MH-SNOM to perform a polarization and phase-resolved optical measurement on a nanostructure in the near-field. It provides a method to compensate the polarization distortion in the MH-SNOM measurement using an isotropic region in the vicinity of the nanostructure as a polarization calibration reference. This algorithm makes the MH-SNOM a very powerful tool for the polarization-resolved characterization of photonic nanostructures with subwavelength-scale resolution. With this algorithm, we succeeded in retrieving experimentally, in three spatial dimensions, the polarization dependent near-field confinement of the optical fields in a form-birefringent grating nanostructure. The obtained measurements are in good qualitative agreement with the theoretical predictions computed with RCWA. In particular, the MH-SNOM measurements verify the predicted polarization-dependent localization of the fields in the near-field regime of the form-birefringent grating, with the TE fields localized in the high-

#173422 - $15.00 USD Received 27 Jul 2012; revised 17 Sep 2012; accepted 18 Sep 2012; published 24 Sep 2012
(C) 2012 OSA

index regions of the FBG, and the TM fields localized in the low-index regions. Moreover, pseudo-far-field measurements demonstrate the effectiveness of the algorithm in the characterization of the effective refractive index of the FBG. Although the algorithm does require a reference flat area for calibration, we have shown that an unstructured region of the device under study is sufficient and should be available with most devices. Thus, this method greatly expands the applicability of the MH-SNOM for the polarization-resolved characterization of photonic nanodevices, potentially assisting in the development of novel devices based on optical nanostructures.

Acknowledgments

This work is supported by the Swiss National Science Foundation (SNSF).

#173422 - $15.00 USD Received 27 Jul 2012; revised 17 Sep 2012; accepted 18 Sep 2012; published 24 Sep 2012
(C) 2012 OSA